Strain-Path Change Tests and Physically Based Polycrystalline Modeling of the Behavior of Recrystallized Zirconium Alloys

Fabien Onimus, Matthew Bono, Jerome Garnier, Annie Soniak-Defresne, Roger Limon, Didier Gilbon, Florent Bourlier, Antoine Ambard

F. Onimus, M. Bono, J. Garnier, A. Soniak, R. Limon, D. Gilbon, F. Bourlier, A. Ambard, Strain-path change tests and physically based polycrystalline modelling of the behavior of recrystallized zirconium alloys. Zirconium in the Nuclear Industry: 18th International Symposium. ASTMP STP Vol. 1597. Eds. R. J. Comstock & A.T. Motta. ASTM International, West Conshohocken, PA, 2018, pp. 180-213.

Symposium : ASTM International B10 18th International Symposium on Zirconium in the Nuclear Industry, May 15-19, 2016, The Westin Hilton Head Island Resort and Spa Hilton Head, SC, USA.

Strain-path change tests and physically based polycrystalline modelling of the behavior of recrystallized zirconium alloys

Authors: *F. Onimus[1*], M. Bono[2], J. Garnier[1], A. Soniak[2], R. Limon[2], D. Gilbon[3], F. Bourlier[4], A. Ambard[5]*

[1]CEA, DEN, Section for Applied Metallurgy Research, 91191 Gif-Sur-Yvette, Cedex, France,

[2]CEA, DEN, Section for Study of Irradiated Materials, 91191 Gif-Sur-Yvette, Cedex, France,

[3]CEA, DEN, Nuclear Material Department, 91191 Gif-Sur-Yvette, Cedex, France,

[4]AREVA NP, 10 rue Juliette Récamier 69456, Lyon Cedex 06, France,

[5]EDF/R&D, Les Renardières, Ecuelles, 77818 Moret sur Loing Cedex, France.

** corresponding author : fabien.onimus@cea.fr*

Zirconium alloys used as cladding tubes for the fuel of Pressurized Water Reactors can undergo high applied stress during power transients. In these conditions, biaxial loading may lead to plastic deformation of the cladding. A comprehensive understanding of the material mechanical response during loading-path change tests is an important step toward the prediction of the behavior in these specific conditions.

Using a non-standard mechanical testing machine, loading-path change tests have been conducted at 623 K on as-received recrystallized Zircaloy-4 tubes. These tests consist of an axial tensile loading and unloading followed by an internal pressure (or pure hoop tension) loading and unloading.

These tests are able to examine the kinematic and isotropic hardening components of the strain hardening behavior of the thin cladding tubes. The isotropic hardening is attributed to dislocation multiplication and dislocation - dislocation interactions. The kinematic hardening is attributed to the interaction of the grains with each other.

A polycrystalline model has also been used and improved in order to simulate the tests. A good prediction of the isotropic and kinematic hardening is provided by the modeling.

Keywords: zirconium alloys, mechanical behavior, strain hardening, kinematic hardening, anisotropy, biaxiality

Introduction

Zirconium alloy tubes are used in the nuclear industry as fuel cladding in pressurized water reactors. Since the cladding is the first confinement barrier against the dissemination of radioactive species, it is of prime importance to guaranty its mechanical integrity throughout its life time. During normal operating conditions, the cladding undergoes a creep down toward the pellet, due to the external pressure of the coolant, progressively reducing the gap between the cladding and the pellet. At the same time, the pellet swells. Eventually, the pellet and the cladding touch each other [1]. Once this contact occurs, the deformation of the cladding follows that of the pellet.

Because of the increasing use of intermittent renewable electricity sources, utilities tend to maneuver nuclear reactors more frequently, which often requires relatively fast power variations [2]. However, during these power transients, the pellet, which expands rapidly due to gaseous swelling and thermal expansion, can apply significant stresses on the cladding [3]. These high stresses may lead to irreversible plastic deformation of the cladding. Furthermore, the stress state is biaxial, and the strain path can be complex depending on the linear power history. A good knowledge and prediction of the effect of loading path changes on the behavior of zirconium alloys is therefore required.

In order to study the response of the material to changes in the loading path, non-standard tests have been proposed. These tests are not representative of a loading that may occur inside the reactor, where creep, stress relaxation and even irradiation creep occur. These tests aim to evaluate, on thin tubes, the various components of the strain hardening behavior, its anisotropy and more generally how the material reacts to significant changes of loading path, in relationship with the deformation mechanisms.

The mechanical behavior of materials is often analyzed, and modeled [4, 5, 6, 7], using the concept of a yield surface. In this framework, the strain hardening is the result of the expansion of the yield surface, which is called “isotropic” hardening, and the translation of the yield surface, which is referred to as “kinematic” hardening. One common example of kinematic hardening is the Bauschinger effect during cyclic tension-compression tests, where a test conducted in tension can lead to a reduced yield stress in subsequent compression, when compared to the yield stress measured in compression without previous tension.

In the case of zirconium alloys, it has been demonstrated by several authors, mainly by using tension-compression tests on thick tubes or thick specimens, that the Bauschinger effect is strong, thus proving that the kinematic hardening is significant [8, 9, 10, 11, 12]. However, it is difficult to perform this type of test on thin tubes, which are susceptible to buckling in compression. Consequently, there are no reported experimental studies of how thin Zircaloy tubes react to significant change of loading path.

As a consequence, the current study performs a new type of test on recrystallized Zy-4 thin tubes, in which the loading path is changed using a succession of steps of axial tension and hoop tension (or

internal pressure tests). This type of test is able to provide some new insights on the strain hardening behavior of thin tubes made of zirconium alloys.

Furthermore, a polycrystalline model able to describe and predict the mechanical behavior of the material has been developed [13, 14]. This model treats the material as an aggregate of crystalline grains. It follows a more predictive modeling approach, compared to classical macroscopic models, by taking into account the crystallographic texture of the material, the interaction of the grains and the microscopic deformation mechanisms.

The objective of this study is to identify the kinematic and isotropic strain hardening behavior of zirconium alloys using strain-path change experiments on thin tubes of recrystallized Zy-4. The experimental data are then compared to a polycrystalline model for the material behavior and are discussed in relation to the deformation mechanisms.

Experimental details

Materials studied

The material studied is a recrystallized zirconium alloy referred to as Zircaloy-4 (Zy-4). This alloy is used in reactors, in the recrystallized metallurgical state, for the grids and the guide tubes of PWR fuel assemblies. However, for cladding tubes, this alloy is used in the stress-relieved metallurgical state. Nevertheless, M5^{TM} alloy, which is in recrystallized state, tends to replace progressively the use of stress-relieved Zy-4 in the AREVA fuel assemblies. Recrystallized Zy-4 is therefore believed to be a good model alloy for recrystallized zirconium alloy, considering the mechanical behavior. Most of the conclusions of this paper can therefore be extended to other recrystallized zirconium alloys such as recrystallized Zy-2 and M5^{TM}.

This material exhibits equiaxed grains with a typical grain size of 6 µm. The crystallographic texture of this material is also typical of recrystallized zirconium alloys in the form of thin cold rolled tubes with the maximum density for the $\{0002\}$ poles in the hoop (noted TD on Figure 1) – radial plane with the maximum pole density tilted at 30° to the radial direction (Figure 1).

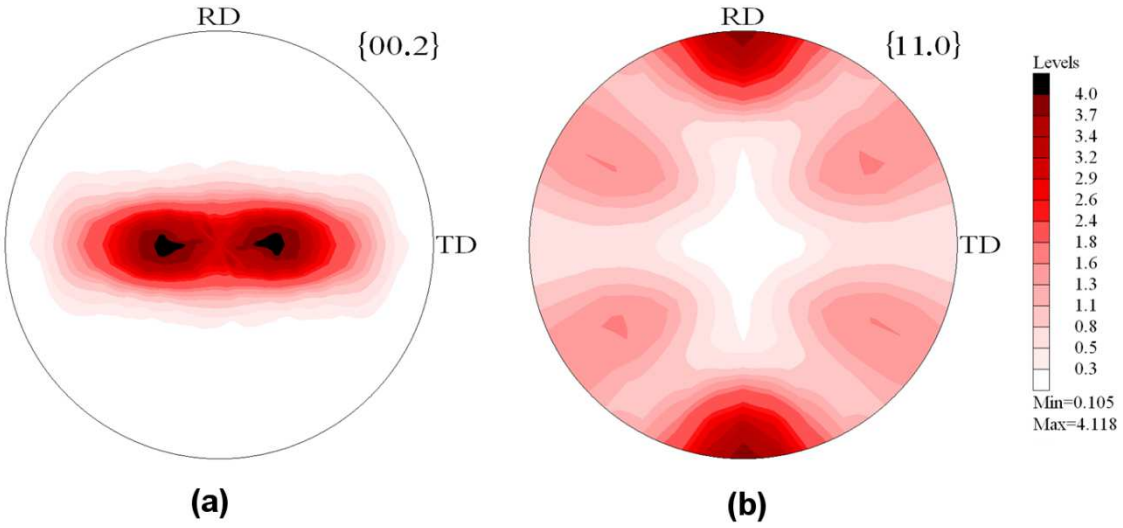

Figure 1: a) {0002} pole figure and b) {$11\bar{2}0$} pole figure of a recrystallized zirconium alloy thin tube. TD refers to the transverse or hoop direction and RD refers to the rolling or axial direction of the tube.

Mechanical testing machine, sample geometry, and mechanical tests

The testing machine [15] is able to apply simultaneously a tensile or compressive force on the tube and an internal pressure via pressurized oil. Thus, biaxial mechanical loading can be achieved where both an axial stress (σ_{zz}) and a hoop stress $(\sigma_{\theta\theta})$ can be applied simultaneously or successively on the same sample. For these tests, it is convenient to define a biaxiality ratio (α) as: $\alpha = \sigma_{zz} / \sigma_{\theta\theta}$. In order to study the effect of a change in the loading path, we have performed successive loadings and unloadings with a given biaxiality ratio followed by a loading-unloading with another biaxiality ratio.

The samples are tubes with a typical thickness of 0.57 mm and typical external diameter of 9.5 mm. The tubes are 90 mm long. The axial force is applied on the tube thanks to a conventional servo-hydraulic testing device. The pressure in the tube is controlled by a hydraulic cylinder. The capacitive extensometers have been provided by Epsilon Company. They are able to operate up to 673 K. The axial extensometer has a gauge length of 50 mm. The hoop extensometer has a gauge length corresponding to the initial diameter of the tube (9.5 mm). Both extensometers are clipped to the sample and installed inside the furnace (Figure 2). Three thermocouples are also installed inside the furnace. The one in the middle of the tube is used for the temperature control. An appropriate grip system has been designed using welded conical end-caps in order to allow simultaneous internal pressure and tension- compression loads to be applied (Figure 2).

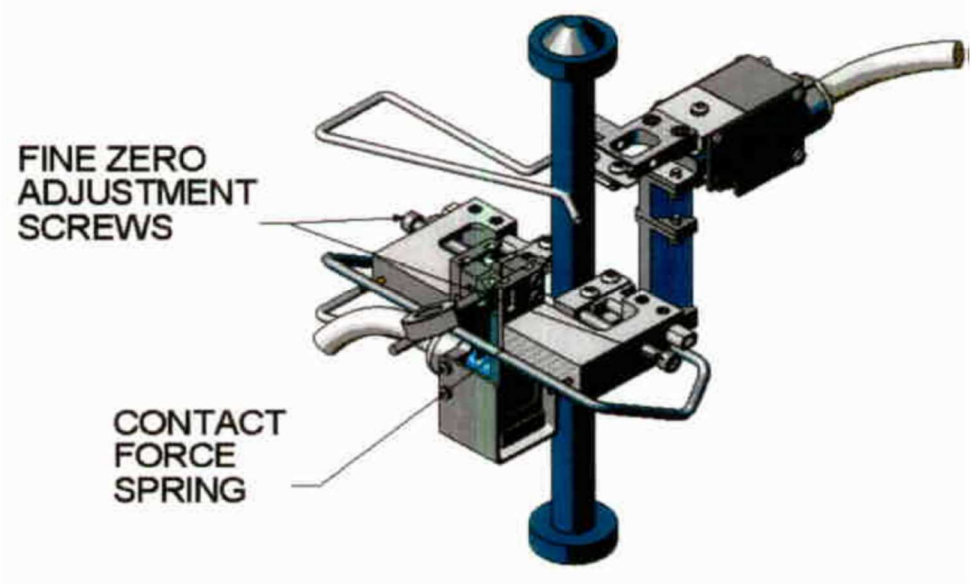

Figure 2: Axial and hoop capacitive extensometers clipped to the sample operating inside the furnace.

When only an internal pressure (IP) is applied to the tube (no additional external axial force), because of the effect of the internal pressure on both ends of the tube, the stress is biaxial, the biaxiality ratio being equal to $\alpha = \sigma_{zz} / \sigma_{\theta\theta}$ =0.47 (see the Appendix).

Because the machine can apply an external compressive axial force in addition to the internal pressure, it is possible to conduct mechanical tests with pure hoop stress (Hoop Tension, HT). Indeed, if the accurately controlled external axial compressive force balances exactly the axial tension force due to the internal pressure on the ends of the tube, then the axial stress in the wall of the tube is equal to zero ($\sigma_{zz} = 0$) and the biaxiality ratio is $\alpha = \sigma_{zz} / \sigma_{\theta\theta}$ =0.

The third studied loading direction is the simple axial tensile test (AT). In this case, the biaxiality ratio should be infinite, but because of a software constraint, a biaxiality ratio of $\alpha = \sigma_{zz} / \sigma_{\theta\theta}$ =100 has been adopted.

The test referred to as AT-HT starts with a loading in the axial direction (AT) (with a biaxiality ratio of $\alpha = \sigma_{zz} / \sigma_{\theta\theta}$ =100), followed by an unloading, then followed by a loading in the pure hoop direction (HT) ($\alpha = \sigma_{zz} / \sigma_{\theta\theta}$ =0), followed by an unloading. This sequence is repeated twice. In this case, a target total strain of 2% is imposed at each step in the axial direction for axial tensile tests and in the hoop direction for pure hoop loading and internal pressure tests. The test referred to as AT-IP starts with a loading in the axial direction (with a biaxiality ratio of $\alpha = 100$), followed by an unloading, then followed by an internal pressure loading ($\alpha = 0.47$), followed by an unloading. This sequence is

repeated twice. The test referred to as HT-AT starts with a loading in the pure hoop direction ($\alpha = 0$), followed by an unloading, then followed by a loading in the axial direction ($\alpha = 100$), followed by an unloading. This sequence is repeated twice. The test referred to as IP-AT starts with an internal pressure loading ($\alpha = 0.47$), followed by an unloading, then followed by a loading in the axial direction ($\alpha = 100$), followed by an unloading. This sequence is repeated twice. All the mechanical tests have been conducted at 623 K. The tests have been conducted with a constant strain rate of 3×10^{-4} s^{-1} in the hoop direction for the internal pressure and pure hoop tensile tests and with a constant strain rate of 3×10^{-4} s^{-1} in the axial direction for the axial tensile tests. The details concerning the mechanical tests performed are listed in Table 1.

The non-standard tests proposed in this work have some analogy with the tests conducted by McEwen et al. [8] for their study of the Bauschinger effect in Zircaloy-2 at room temperature.

Table 1: Mechanical tests performed on recrystallized Zy-4.

	AT-HT		AT-IP		HT-AT		IP-AT	
Step	Biaxiality ratio	Maximum total strain	Biaxiality ratio	Maximum total strain	Biaxiality ratio	Maximum total strain	Biaxiality ratio	Maximum total strain
1	α=100	2%	α=100	2%	α=0	2%	α=0.47	2%
2	α=0	2%	α=0.47	2%	α=100	2%	α=100	2%
3	α=100	2%	α=100	2%	α=0	2%	α=0.47	2%
4	α=0	2%	α=0.47	2%	α=100	2%	α=100	2%

The formula used to analyze the mechanical tests have been partly given in [16, 17] and are detailed in the Appendix. This is referred to as the "quasi-biaxial" approach. In this framework, the hoop stress and axial stress are defined as $\sigma_{\theta\theta}^{qb} = \sigma_{\theta\theta} - \sigma_{rr}$ and $\sigma_{zz}^{qb} = \sigma_{zz} - \sigma_{rr}$ (see Appendix). The true stresses and strains are used in the analysis.

The plastic strain tensor components are computed by subtracting the elastic deformation from the total deformation. Elastic deformation is calculated using Hooke's law (equation 1) assuming isotropic elasticity with the Young's modulus (E) and the Poisson's ratio (ν).

$$\underline{\underline{\varepsilon}}^{p} = \underline{\underline{\varepsilon}} - \underline{\underline{\varepsilon}}^{e} = \underline{\underline{\varepsilon}} - \frac{1}{E}\left[(1+\nu)\underline{\underline{\sigma}} - \nu\,\mathrm{tr}(\underline{\underline{\sigma}})\underline{\underline{I}}\right] \quad (1)$$

The true stress is plotted as a function of the true plastic strain. Furthermore, in order to compare the tests with each other, the stress –plastic strain curves have been translated so that the beginning of each step of the test starts with zero plastic strain. This is referred to as the translated plastic strain. Moreover, in order to have a better understanding of the effect of the cumulated plastic strain on the

behavior of the material, an equivalent cumulated plastic strain has been computed. The equivalent cumulated plastic strain is generally defined using equation 2.

$$\varepsilon_{eq}^{p} = \int_{0}^{t} \dot{\varepsilon}_{eq}^{p} dt = \int_{0}^{t} \sqrt{\frac{2}{3} \dot{\underline{\underline{\varepsilon}}}^{p} : \dot{\underline{\underline{\varepsilon}}}^{p}} \, dt \quad (2)$$

In this work, it has been chosen to compute the equivalent cumulated plastic strain by assuming an isotropic behavior rather than computing the anisotropic experimental equivalent cumulated plastic strain. During each axial tensile test, the increment in equivalent plastic strain is thus given by equation 3. For each internal pressure test, it is given by equation 4. The simplified expression given by equation 5 is used for the pure hoop tensile tests. The equivalent cumulated plastic strain is then computed by adding the equivalent plastic strain increment for each step. This computation is done in exactly the same way to analyze the experiments and the numerical simulations.

$$\Delta\varepsilon_{eq}^{p} = \Delta\varepsilon_{zz}^{p} \quad (3)$$

$$\Delta\varepsilon_{eq}^{p} = \frac{2}{\sqrt{3}} \Delta\varepsilon_{\theta\theta}^{p} \quad (4)$$

$$\Delta\varepsilon_{eq}^{p} = \Delta\varepsilon_{\theta\theta}^{p} \quad (5)$$

Furthermore, with this equivalent plastic strain computed for isotropic behavior, it is possible to evaluate the flow stress for different equivalent plastic strain offsets. The strain offsets chosen are: $\Delta\varepsilon_{eq}^{p}$ = 0.1%, 0.2%, and 1.0%.

Experimental results

Analysis of the strain path

Figure 3 shows the evolution of the axial strain as a function of the hoop strain (the continuous lines) for the four tests conducted on recrystallized Zy-4. From these plots, the strain path ($\dot{\varepsilon}_{zz} / \dot{\varepsilon}_{\theta\theta}$) can be evaluated for each test. From these values, the angle θ (measured counterclockwise) between the x-direction, of the hoop strain - axial strain plot, and the strain rate vector can be computed as $\theta = \arctan\left(\dot{\varepsilon}_{zz} / \dot{\varepsilon}_{\theta\theta}\right)$ if $\dot{\varepsilon}_{\theta\theta}$>0 (for $\dot{\varepsilon}_{zz}$>0 or $\dot{\varepsilon}_{zz}$<0), $\theta = \pi + \arctan\left(\dot{\varepsilon}_{zz} / \dot{\varepsilon}_{\theta\theta}\right)$ if $\dot{\varepsilon}_{\theta\theta}$<0 and $\dot{\varepsilon}_{zz}$>0, $\theta = \arctan\left(\dot{\varepsilon}_{zz} / \dot{\varepsilon}_{\theta\theta}\right) - \pi$ if $\dot{\varepsilon}_{\theta\theta}$<0 and $\dot{\varepsilon}_{zz}$<0. For the eight axial tensile tests, the strain path ranges from -1.03 to -1.22 (angle θ ranging from 129° to 134°). For the four pure hoop tensile tests, the strain path ranges from -0.76 to -0.80 (angle θ ranging from -37° to -39°). For the four internal pressure tests, the strain path ranges from -0.33 to -0.38 (angle θ ranging from -18° to -21°). When pure hoop tensile tests and axial tensile tests are conducted alternately, the strain paths are nearly opposite to each other, the angle between these two directions being close to 170°. On the other hand, when

internal pressure tests and axial tensile tests are conducted alternately, the angle between these two directions is close to 150°.

As shown in figures 3b and 3d, during internal pressure steps, the axial strain decreases significantly. This illustrates the significant plastic anisotropy of the material since an isotropic behavior should lead to a zero axial strain rate.

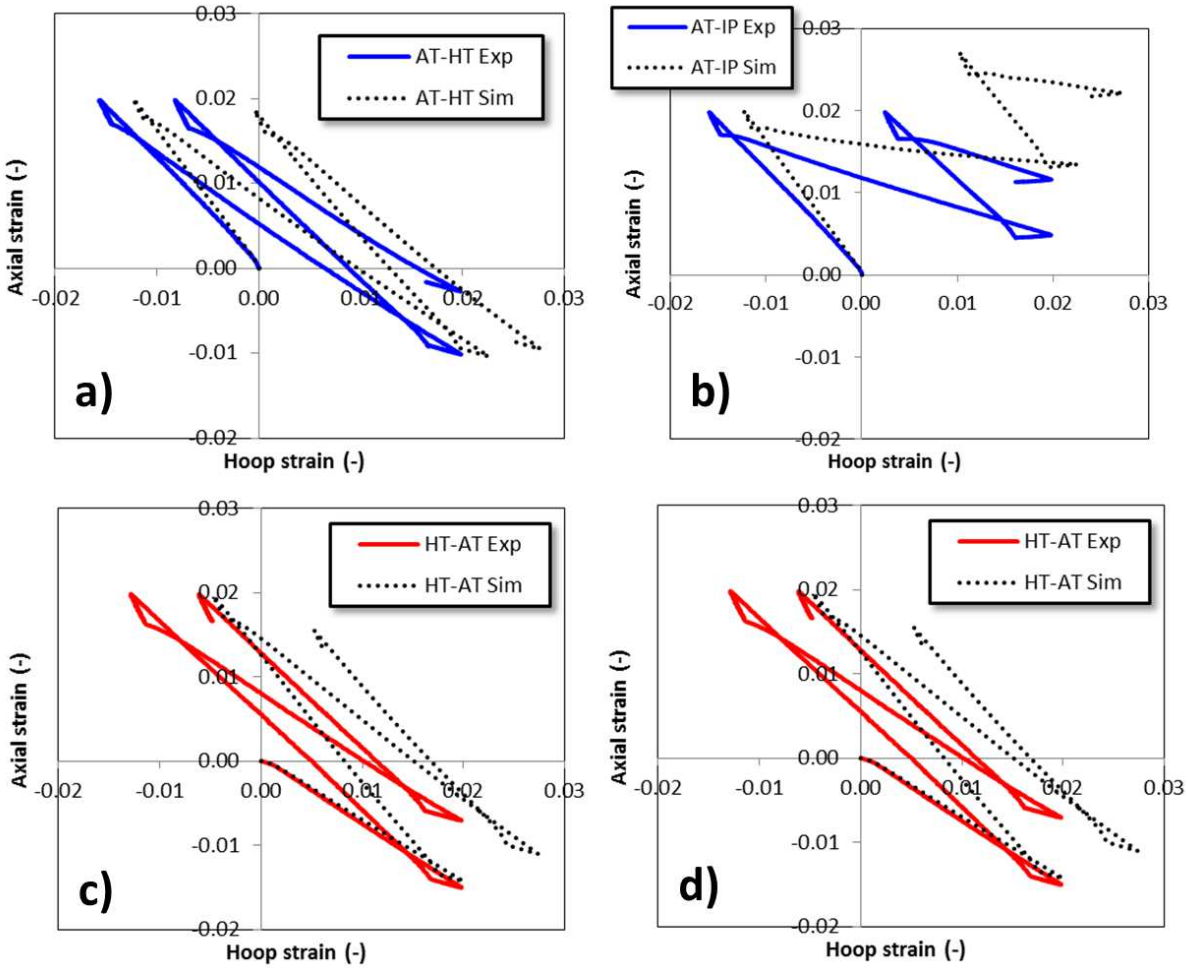

Figure 3: Strain path (axial strain vs. hoop strain) for the four tests performed on the non-irradiated recrystallized Zy-4. The experimental strain path is shown by the continuous lines. AT-HT and AT-IP tests are shown in blue lines. HT-AT and HT-IP tests are shown in red lines. The simulated strain path is shown by the black dotted lines.

Evaluation of the elastic properties

For the axial tensile tests, the Young's modulus measured during the first step is equal to 80 GPa. For the internal pressure test performed as the first step (test IP-AT), the measured elastic slope is 103 GPa. According to the formula given in Appendix, and assuming isotropic elasticity, the Poisson's ratio is then equal to 0.34.

The Poisson's ratio can also be evaluated from the strain path ($\dot{\varepsilon}_{zz}/\dot{\varepsilon}_{\theta\theta}$) measured in the elastic domain. It is especially convenient in the case of the internal pressure test (first step of test IP-AT) where a reversal in the axial strain rate, starting positive in the elastic domain and becoming negative in the plastic domain, can be observed (Figure 3d). From this measurement, a Poisson's ratio equals to 0.39 is found. The Poisson's ratio can also be evaluated for the axial tensile tests, for which values of 0.45 and 0.48 are obtained. The discrepancies between these various results are due to the limited experimental accuracy but also to the anisotropic elastic behavior of zirconium alloys.

From their experiments on Zy-4 containing 1000 ppm oxygen, Northwood et al. [18] found a Young's modulus of 77 GPa at 350°C. A value of 78 GPa at 350°C is also obtained by Delobelle et al. [11] on recrystallized Zy-4, in good agreement with our experiments.

At 315°C, Schwenk et al. [19] obtained a Poisson ratio of 0.41. This parameter does not seem to evolve much with temperature. For their modeling, Delobelle et al. [11] used a Poisson's ratio of 0.4 at 350°C for recrystallized Zy-4. This value of 0.4 for the Poisson ratio seems rather high compared to other alloys but it is the results of the anisotropic elastic behavior of zirconium alloys as shown in [20]. In our analysis, we used a value of 80 GPa for the Young's modulus and 0.4 for the Poisson's ratio.

Analysis of the kinematic and isotropic hardenings

The effect of the kinematic hardening on the evolution of the yield surface is shown in Figure 4. It can be seen on this schematic that for a pure kinematic hardening behavior, if an axial tensile loading is conducted first, then the yield stress, measured when conducting a subsequent pure hoop tensile test, is reduced. The same should also be true when reversing the order of the two tests.

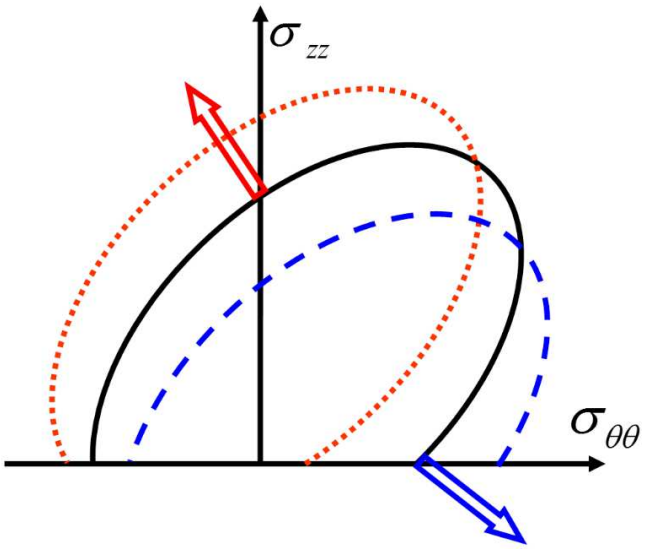

Figure 4: Schematic showing the translation of the yield surface under axial tensile loading or under pure hoop tensile loading if only kinematic hardening is active.

Figure 5 shows a comparison between the first step and the second step conducted with pure hoop loading (HT), axial tensile loading (AT), and internal pressure loading (IP). On these plots, the stress (hoop or axial) is represented as a function of the translated plastic strain (hoop or axial). The first steps are shown as continuous lines and the second steps are shown as dotted lines. Tests starting with axial tests (AT-HT and AT-IP tests) are shown in blue lines whereas tests finishing by axial tests (HT-AT and IP-AT tests) are shown in red lines. These plots highlight the effects of the prior tests. Two main effects of the prior tests can be noted. First, it can be seen, when comparing step 2 of test AT-HT to step 1 of test HT-AT (Figure 5b), that the yield stress in pure hoop tension, has been reduced by the prior axial tensile test. This phenomenon is an indication of kinematic hardening, as explained by the schematic in Figure 4. This phenomenon is not as clearly observed when considering the internal pressure tests and the axial tensile tests. Furthermore, it is noticed that the flow stress reached after 1.5% translated plastic strain is systematically higher for the second steps than for the first steps (Figure 5). This is due to the isotropic hardening that occurs when the cumulated equivalent plastic strain increases. It is also worth pointing out, when comparing Fig. 4a and Fig. 4c, that this isotropic strain hardening is stronger when the axial test is performed after an internal pressure test (IP-AT) than after a pure hoop tensile test (HT-AT).

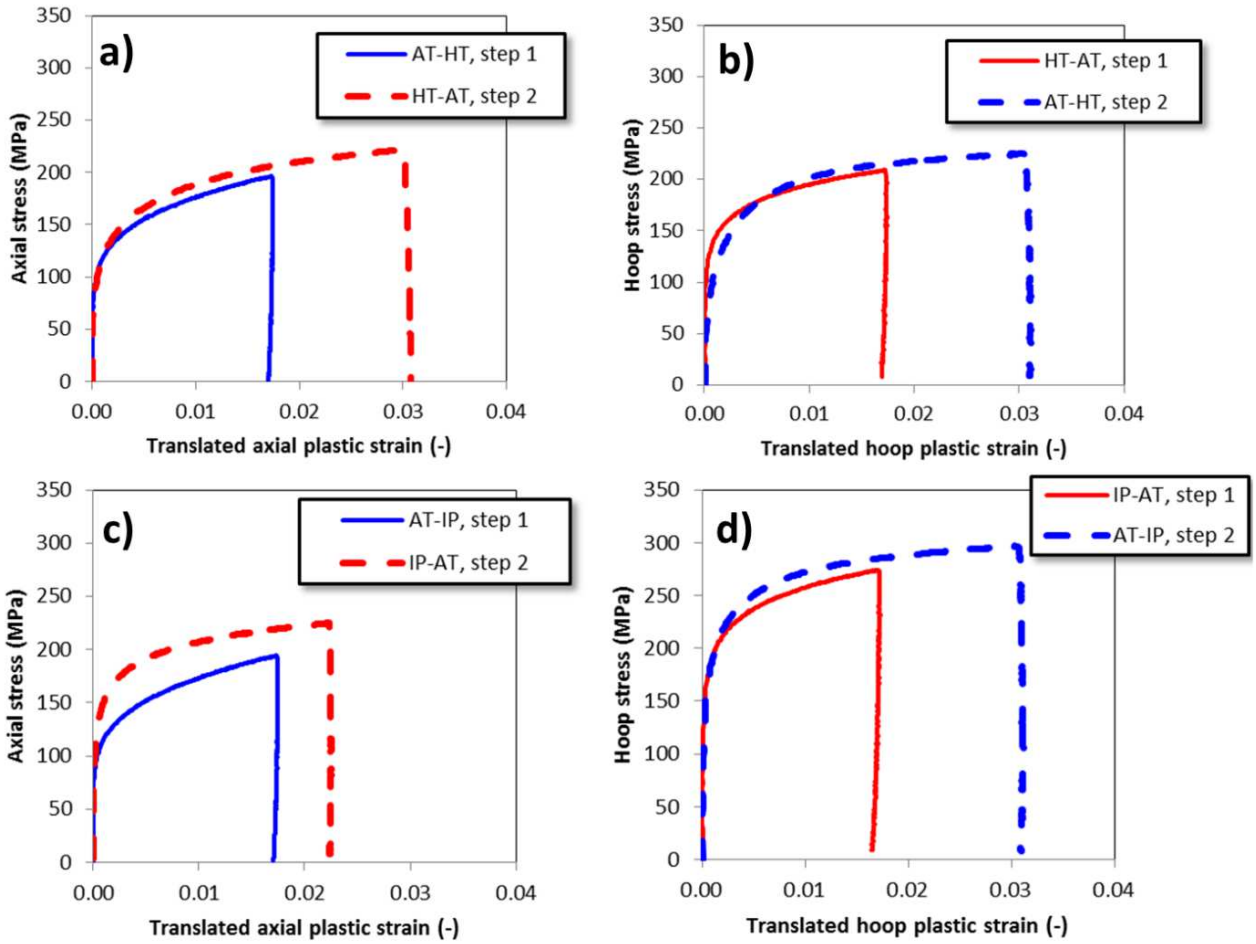

Figure 5: Comparison between the first and second steps of a) axial tensile tests, b) pure hoop tensile tests, c) axial tensile tests and d) internal pressure tests. The stress is shown as a function of the translated plastic strain. The first steps are shown as continuous lines and the second steps are shown as dotted lines. The AT-HT and AT-IP tests are shown in blue lines and the HT-AT and IP-AT tests are shown in red lines.

The effect of the cumulated plastic strain can be more clearly seen when plotting the stress (axial or hoop) as a function of the cumulated equivalent plastic strain for each test (Figures 6 and 7). It can be observed that the flow stress increases progressively as the cumulated equivalent plastic strain increases which is an indication of isotropic hardening.

It should be mentioned that during pure hoop tensile tests, a small axial stress appears because it is the so-called "quasi-biaxial" axial stress (defined as $\sigma_{zz}^{qb} = \sigma_{zz} - \sigma_{rr}$) that is plotted on the vertical axis. Indeed, for this test, the ratio between the axial and the hoop "quasi-biaxial" stresses is $\sigma_{zz}^{qb} / \sigma_{\theta\theta}^{qb} =$ 0.064.

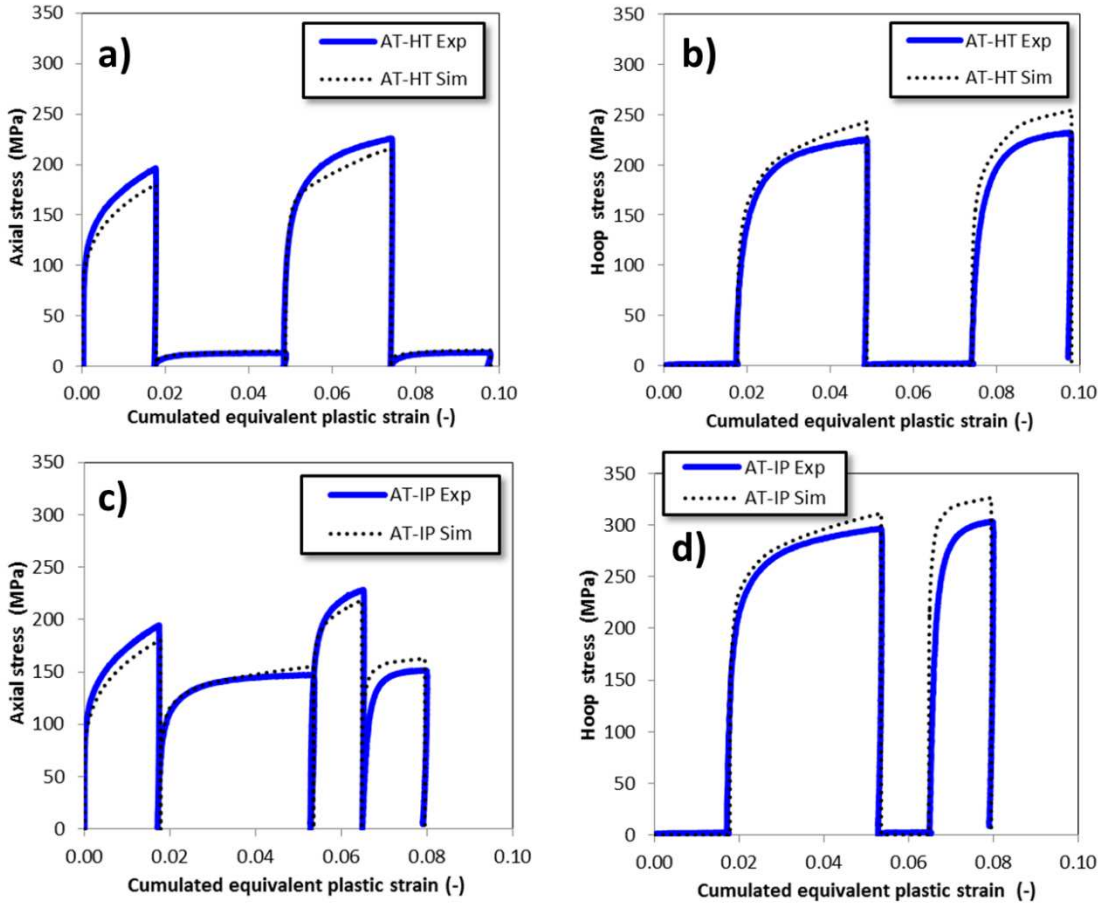

Figure 6: Stress (hoop or axial) as a function of the cumulated equivalent plastic strain for two tests conducted on recrystallized Zy-4 starting with axial test. The AT-HP test is shown on a) and b). The AT-IP test is shown on b) and c). The experimental results are shown as continuous blue lines. The results of the simulation are shown as a black dotted line.

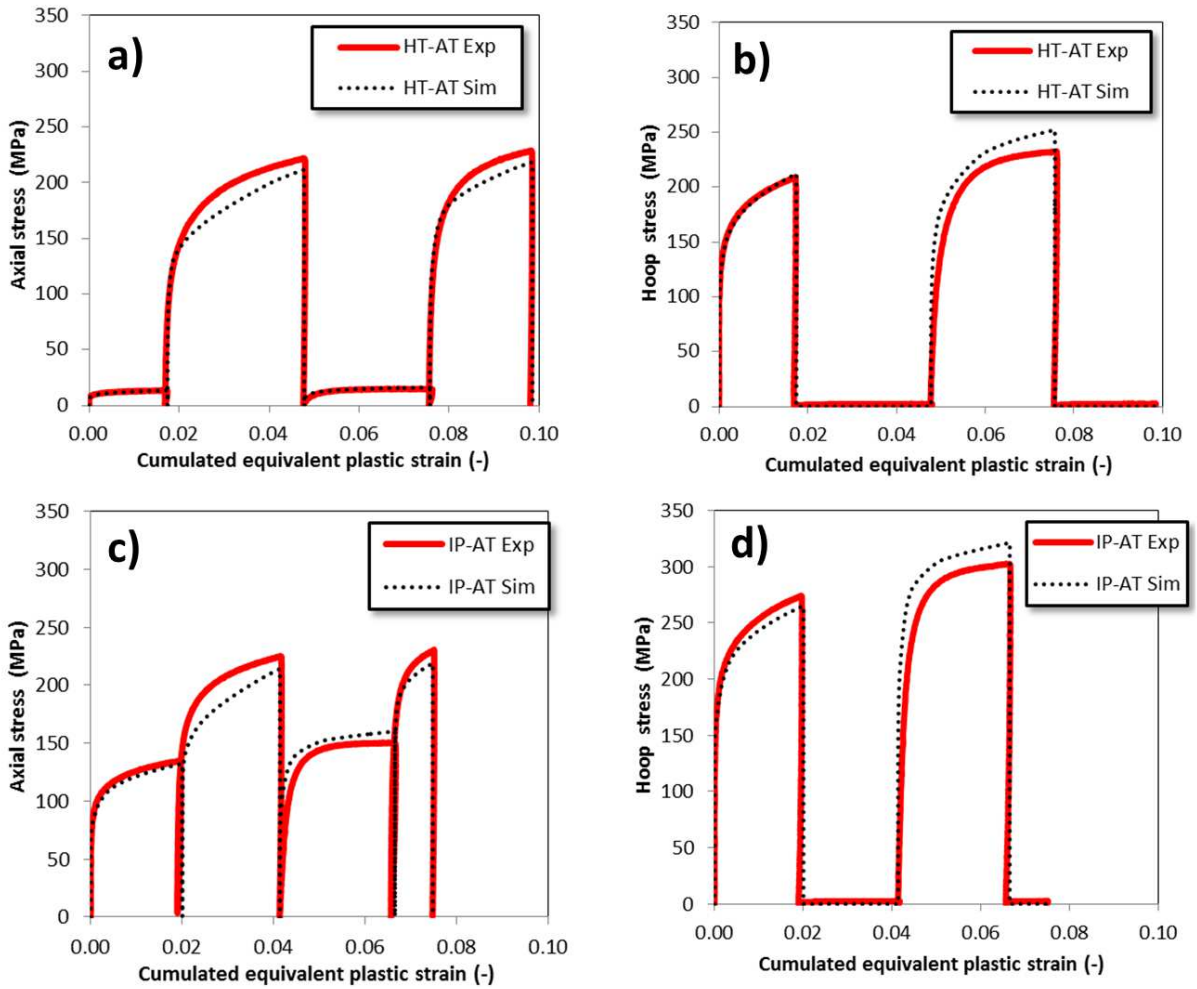

Figure 7: Stress (hoop or axial) as a function of the cumulated equivalent plastic strain for the tests (HT-AT shown in (a) and (b)) and IP-AT (shown in (c) and (d)) conducted on recrystallized Zy-4 starting . The experimental results are shown as continuous red lines. The results of the simulation are shown as a black dotted line.

In order to analyze in more detail the kinematic and isotropic hardening, the flow stress at several offset values for the equivalent plastic strain has been measured from the stress-strain curves. These values are reported as a function of the cumulated equivalent plastic strain in Figures 8.

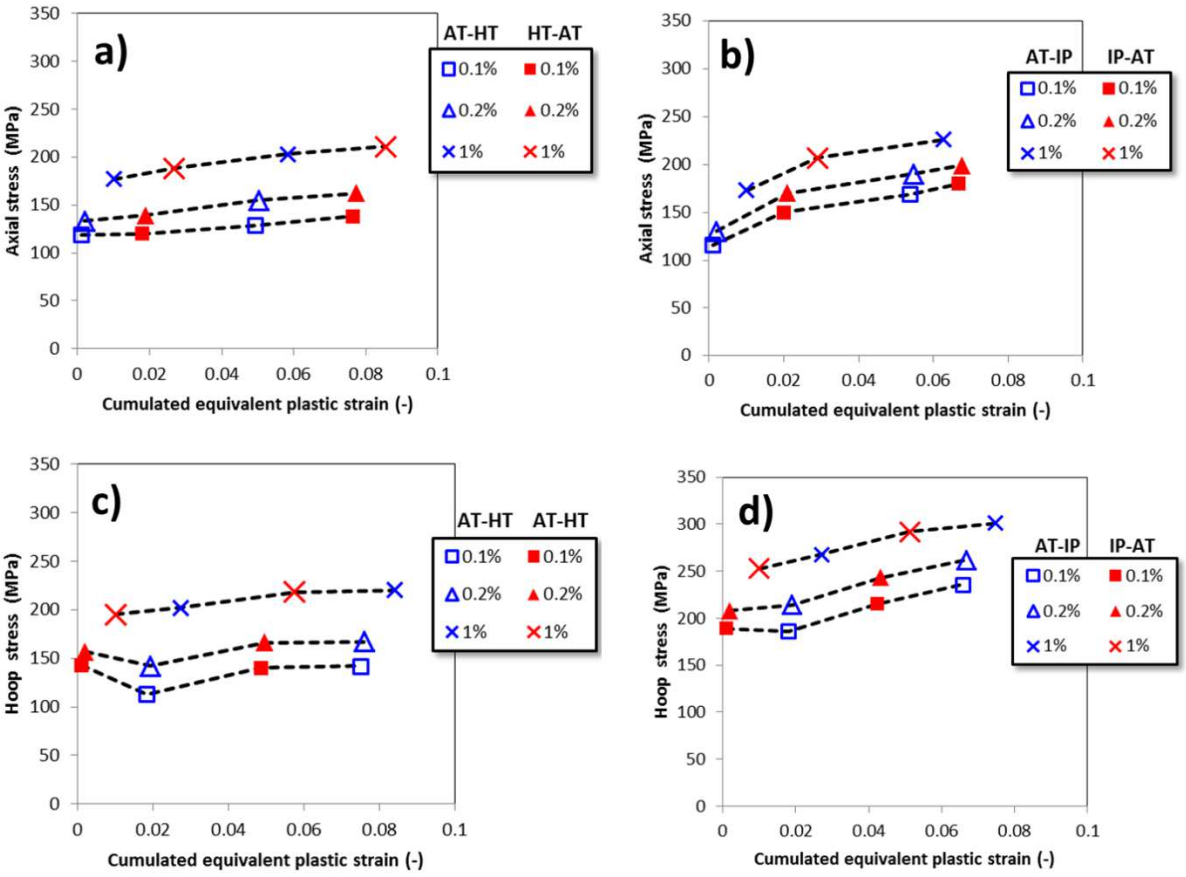

Figure 8: Evolution, as a function of the cumulated equivalent plastic strain, of the flow stress (axial or hoop) measured for several equivalent plastic strain offsets for non-irradiated Zy-4. a) and c) show the flow stresses for the tests AT-HT and HT-AT measured in the axial (a) and hoop directions (c). b) and d) show the flow stresses for the tests AT-IP and IP-AT measured in the axial (b) and hoop directions (d).

These plots show that the flow stress measured for a small plastic strain offset (0.1%) exhibits a significant decrease between the first and the second steps for the pure hoop tensile test (Figure 8c). As stated above, this is due to the kinematic hardening. The same seems to be true for the internal pressure test, but to a lesser extent (Figure 8d). This phenomenon is not observed for the axial tensile tests (Figure 8a and 8b). For higher plastic strain offsets, an increase in flow stress is always observed (Figure 8). This is due to the isotropic hardening.

As pointed out by several authors [21, 22], the analysis of the unloading may also give some information concerning the magnitude of the kinematic hardening. Indeed, during the unloading, a phenomenon similar to the Bauschinger effect may be observed, in specific conditions.

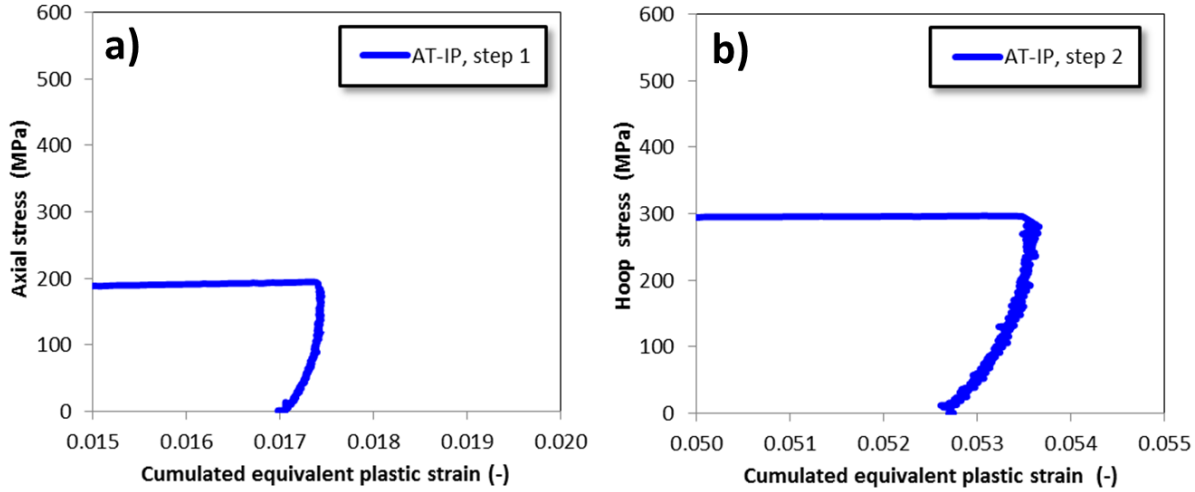

Figure 9: Enlarged view of the unloading of AT-IP steps 1 (a) and 2 (b), over a strain range of 0.5%, at the same scale.

For this analysis, it is necessary to define two new values: the kinematic stress tensor ($\underline{\underline{X}}$) which is associated to the translation of the yield surface and the isotropic stress (R), associated to the size of the yield surface. If the kinematic stress component in the considered loading direction exceeds the isotropic stress, plastic deformation can occur at the end of the unloading [21]. This phenomenon is evidenced by a non-linearity on the stress-strain curve during the unloading. This is best evidenced when the stress is plotted as a function of the plastic strain (or cumulated equivalent plastic strain). The Figure 7c and 7d showing the stress as a function of the cumulated equivalent plastic strain have been enlarged, on Figure 9a and 9b, over a strain range of 0.5% to show the unloading of the step 1 of the test AT-IP and the unloading of the step 2 of the test AT-IP, as an example. In Figure 9, a significant non-linearity of the unloading is observed, which proves that the kinematic stress component (X) is higher than the isotropic stress (R) in these loading directions. The quantitative evaluation of the kinematic and isotropic stress by this method remains tricky since the non-linearity is progressive. Furthermore, experimental artifacts may also arise at the end of the unloading that could also induce a non-linearity on the stress-plastic strain curve. As a consequence this type of analysis should be considered with care.

Analysis of the anisotropic yield surface

From the three loading directions studied in this work, the anisotropy of the yield surface can be evaluated. As a first approximation, it is assumed that the yield surface follows a Hill's criterion [23, 24]. With this assumption, the Hill's equivalent stress can be written as equation 6, within the quasi-biaxial approach detailed in the Appendix.

$$\sigma_H^{eq} = \sqrt{H_1\left(\sigma_{\theta\theta}^{qb} - \sigma_{zz}^{qb}\right)^2 + \left(1 - H_1\right)\left(\sigma_{zz}^{qb}\right)^2 + H_3\left(\sigma_{\theta\theta}^{qb}\right)^2} \qquad (6)$$

With this definition, the Hill's equivalent stress during axial tensile test is equal to the axial stress ($\sigma_H^{eq} = \sigma_{zz}^{qb}$). During internal pressure test the Hill's equivalent stress is equal to $\sigma_H^{eq} = \sigma_{\theta\theta}^{qb}\sqrt{H_3 + 1/4}$ and during pure hoop tensile test it is equal to $\sigma_H^{eq} \approx \sigma_{\theta\theta}^{qb}\sqrt{H_3 + H_1(1-2\eta)}$, considering a second order approximation in η ($\eta = 0.064$). The flow stresses measured for an equivalent plastic strain offset equal to 0.1% during the first steps of each of the four tests has been used to compute the H_1 and H_3 coefficients of the Hill's criterion. From the flow stress measured during internal pressure loading (189 MPa for the test IP-AT) and the two values obtained during axial tensile tests (119 MPa for the test AT-HT and 116 MPa for the test AT-IP), the values estimated for the coefficient H_3 are equal to 0.15 and 0.13 respectively. From the flow stress measured during the pure hoop tensile test (143 MPa for the test HT-AT), two values, 0.61 and 0.63, can also be deduced for the coefficient H_1 .

Discussion of the results

The reason for the decrease of the flow stress when comparing hoop tensile tests conducted during the first step of test HT-AT and the second step of test AT-HT (Figure 5b and Figure 8c) is due to the kinematic hardening. Indeed, the prior axial tensile test induces a translation of the yield surface that decreases the yield stress of the subsequent pure hoop tensile test or internal pressure test. This phenomenon is analogous to the Bauschinger effect (as explained in Figure 4). The fact that this phenomenon is more prevalent for pure hoop tension than for internal pressure is related to the angle between the two strain rate vectors in the hoop strain – axial strain plane. For alternating axial tensile and pure hoop tension, the angle between the two strain rate directions is 170°, whereas for alternating axial tensile and internal pressure, it is only 150°. As a consequence, the yield surface is translated in two nearly opposite directions for axial tension and pure hoop tension, whereas this is not the case for internal pressure and axial tension. The effect of the yield surface translation is therefore lower. It is worth pointing out that this phenomenon is not observed during axial tensile tests, although kinematic hardening must also occur in this loading direction.

The Bauschinger effect was clearly observed by McEwen et al. [8] on recrystallized Zy-2 thick samples taken out of a rolled slab after prior compression and then tested at room temperature along the transverse or rolling direction. These authors have shown that a pre-straining in compression along the longitudinal direction leads to a reduction in yield stress in the transverse direction. This is in good agreement with our results where a pre-tension along the longitudinal direction leads to a reduction in yield stress in the hoop (transverse) direction (Figure 8c). Surprisingly, these authors did not show any reduction in yield stress when the pre-straining is done in compression along the transverse direction followed by a tension in the longitudinal direction. This result is also in agreement with our own findings (Figure 8a) where no reduction in yield stress is observed when the pre-straining is conducted in tension along the transverse direction then followed by a tension along the hoop (transverse) direction. These authors also tested a thick specimen taken out of a recrystallized Zy-2 swaged rod at room temperature in tension-compression tests. A very large Bauschinger effect was clearly evident as seen from the hysteresis loops. Delobelle et al. [11] also clearly observed a strong Bauschinger effect at 623 K during tension-compression tests along the axial direction or during tension-torsion tests on thicker tubes (1.2 mm thick) made of recrystallized Zy-4.

In the case of thin cladding tubes, it is difficult to prove the existence of a strong Bauschinger effect although, based on previous literature results, this effect must be present. The new results given here tend to prove the existence of a significant Bauschinger effect in the case of thin cladding tubes made of recrystallized zirconium alloys.

The progressive increase in the flow stress measured for higher plastic strain offsets (Figure 8), when the amount of pre-straining increases (cumulated equivalent plastic strain), is due to the isotropic hardening, which corresponds to a progressive expansion of the yield surface. This isotropic hardening was also observed by McEwen et al. [8]. It should be noticed that this hardening remains limited, as shown on figures 8a and 8c. Indeed, as the equivalent cumulated plastic strain increases up to 8%, the flow stress increases only slightly. This suggests that the isotropic hardening remains low compared to the kinematic hardening. The cyclic tests conducted at 623 K by Wisner et al. [10] on as-received Zy-2 also show a rather low cyclic hardening. This confirms that the isotropic hardening remains limited for recrystallized zirconium alloys.

At the microscopic scale, the isotropic hardening (expansion of yield surface) is usually attributed to the multiplication of dislocations during the plastic deformation and their mutual interactions. During dislocation interactions, junctions are created and act as pinning points. These dislocations, often referred to as forest dislocations, play the role of dispersed obstacles against dislocation glide. Because these obstacles are homogeneously distributed and create a stress field of relatively short range [21, 30], their effect is not “polarized”. In other words, a dislocation gliding in one direction experiences

the same “resistance” due to forest dislocations as it would if it were gliding in the opposite direction [21]. This explains why the forest dislocations induce a so called “isotropic” hardening.
In the case of pure zirconium the increase in yield stress has been clearly correlated to the increase in dislocation density an early study [25] reviewed by Douglass [26]. The increase in yield stress due to the increase of dislocation density also partly explains the higher strength of cold worked stress relieved Zy-4 compared to recrystallized Zy-4 [11]. However, it has been discussed by Monnet et al. [27], using dislocation dynamics simulations, that the forest hardening should remain limited for Zircaloy-4. Indeed, when the mobility of screw dislocations gliding in prismatic planes is smaller than that of edge dislocations in HCP metals, which is believed to be the case for Zircaloy-4, the formation of junctions between intersecting screw dislocations is difficult and therefore the forest hardening is low. This could explain why only a small amount of isotropic hardening was measured in our experiments.

The Bauschinger effect, the most illustrative case of kinematic hardening, corresponds to a “polarization” of internal stresses when comparing tension and compression. This phenomenon can have various origins at the microscopic scale, depending on the material and its microstructure. For instance, it is reported in the literature that dislocation pile-ups or dislocations by-passing precipitates can induce a Bauschinger effect. However, these effects are not observed for recrystallized zirconium alloys. Only homogeneous dislocation glide in the various crystallographic slip planes is usually observed during low strain monotonic tensile testing. The strong Bauschinger effect observed in zirconium alloys must therefore have another origin. It is known, as reviewed in [28], that the easy glide slip system in zirconium is the prismatic slip system with the glide direction along an <a> direction. The only deformation modes that can accommodate the plastic deformation along the <c> direction are <c+a> pyramidal slip and twinning. These two deformation modes are difficult to activate in thin industrial products. Twinning is usually not observed for cladding tubes tested at 623 K, and only <c+a> slip occurs in grains not well orientated for <a> slip. These grains are referred to as the “hard” grains, the “soft” grains being the grains well orientated for <a> slip and especially prismatic slip. In a polycrystal, the neighboring grains interact with each other. The deformation of each grain is therefore affected by its neighbors. The soft grains, which are well orientated for <a> slip, tend to deform plastically, but the hard grains, which are not well orientated for <a> slip, remain elastic and therefore impede the deformation of the soft grains. This leads to a “composite” effect between the “hard” grains and the “soft” grains, which induces strain incompatibilities between grains leading to intergranular internal stresses or back stresses, as described or discussed in [8, 9, 12, 21, 28, 29, 30]. When unloading and compression occur, a Bauschinger effect appears. This is the main origin of the kinematic hardening observed in zirconium alloys.

Polycrystalline Modeling

The polycrystalline model used and improved here has been described elsewhere [13, 14]. The principle of this type of model is to consider the material not as homogeneous but as a heterogeneous medium in the form of a polycrystalline aggregate, the objective being to deduce the effective properties of the polycrystal from knowledge of the behavior of the individual grains [29]. In this model, the crystallographic texture of the material is explicitly taken into account. The microscopic deformation mechanisms are modeled by intra-granular constitutive laws. The model computes how the grains interact between each other, thereby enabling the calculation of the overall behavior of the polycrystal. The inter-granular kinematic hardening and the effect of the texture are therefore outcomes of the model.

The polycrystalline model is based on the so-called mean field approach. In this framework, the detailed spatial organization of the grains is not taken into account. All the grains with the same crystallographic orientation are considered as the same crystallographic phase (g) characterized by its three Euler's angles $(\varphi_1, \phi, \varphi_2)$ and its volume fraction (f_g). Then each crystallographic phase of the polycrystal is successively regarded as an inclusion within a "matrix" made of all the crystallographic phases (homogeneous equivalent medium) subjected to homogeneous boundary conditions. Since the resulting response of a crystallographic phase depends on its interaction with the homogeneous equivalent medium and since the behavior of the homogeneous equivalent medium is the average response over all the crystallographic phases, a self-consistent problem must be solved. In the case of linear elasticity, an exact solution of this problem has been derived based on the resolution of the Eshelby's problem [31]. In the case of non-linear behavior, several approaches have been proposed by various authors [32, 33]. In the case of polycrystals with isotropic texture (assuming isotropic elasticity with Young's modulus E, Poisson's ratio ν, and shear modulus $\mu = E/(2+2\nu)$) and with crystallographic phases that can be considered as spheres within the matrix, Berveiller and Zaoui [34] have proposed a so-called ''secant linearization" of the self-consistent problem. These authors have shown that, in these conditions and under radial monotonic loading, the local stress ($\underline{\underline{\sigma}}_g$) in the crystallographic phase (g) and the macroscopic stress ($\underline{\underline{\Sigma}}$) are related by a simple explicit expression, referred to as the concentration rule, given by equation 7.

$$\underline{\underline{\sigma}}_g = \underline{\underline{\Sigma}} + 2\mu(1-\beta)\left(\underline{\underline{E}}^p - \underline{\underline{\varepsilon}}_g^p\right)\alpha(\underline{\underline{\Sigma}}, \underline{\underline{E}}^p) \qquad (7)$$

Where β is a parameter equal to $\beta = [2(4-5\nu)]/[15(1-\nu)]$ and the function $\alpha(\underline{\underline{\Sigma}}, \underline{\underline{E}}^p)$ is defined by equation 8.

$$\frac{1}{\alpha(\underline{\underline{\Sigma}},\underline{\underline{E}}^p)} \approx 1+\frac{3}{2}\mu\frac{\left\|\underline{\underline{E}}^p\right\|}{J_2\left(\underline{\underline{\Sigma}}\right)} \qquad (8)$$

The notation $J_2\left(\underline{\underline{\Sigma}}\right)$ and $\left\|\underline{\underline{E}}^p\right\|$ are defined as $J_2\left(\underline{\underline{\Sigma}}\right)=\sqrt{\frac{3}{2}\underline{\underline{\Sigma}}:\underline{\underline{\Sigma}}}$ and $\left\|\underline{\underline{E}}^p\right\|=\sqrt{\frac{2}{3}\underline{\underline{E}}^p:\underline{\underline{E}}^p}$, where $\underline{\underline{E}}^p$ is the macroscopic plastic strain tensor and $\underline{\underline{\Sigma}}$ the macroscopic stress tensor.

As pointed out in [35] the model proposed by Berveiller and Zaoui [34] is only suitable for monotonic loading applied to isotropic polycrystals. It does not allow the simulation of changes of loading path for textured polycrystals. In order to keep the advantage of a concentration rule that can be expressed explicitly and in order to extend the field of applications of this type of model, Cailletaud [36] and Pilvin [37, 38, 39] have postulated an explicit concentration rule (equation 9).

$$\underline{\underline{\sigma}}_g=\underline{\underline{\Sigma}}+2\mu(1-\beta)\left(\underline{\underline{B}}-\underline{\underline{\beta}}_g\right) \quad \text{with} \quad \dot{\underline{\underline{\beta}}}_g=\dot{\underline{\underline{\varepsilon}}}_g^p-D\left(\underline{\underline{\beta}}_g-\delta\underline{\underline{\varepsilon}}_g^p\right)\left\|\dot{\underline{\underline{\varepsilon}}}_g^p\right\| \quad \text{and} \quad \underline{\underline{B}}=\sum_{g\in G}f_g\underline{\underline{\beta}}_g \qquad (9)$$

The new second rank tensor internal variable $\underline{\underline{\beta}}_g$ is a local internal variable that evolves non-linearly with the local plastic strain ($\underline{\underline{\varepsilon}}_g^p$) of the crystallographic phase, according to Eq. (9). The tensor formulation is able to give a suitable description of cyclic tests. This polycrystalline model, referred to here as the Cailletaud–Pilvin (C–P) model, is not itself a self-consistent model from the homogenization theory point of view. It has therefore been proposed to adjust the two parameters, D and δ, which govern the evolution of the internal variable $\underline{\underline{\beta}}_g$, on the local response of the model developed by Berveiller and Zaoui [34], referred to as the B-Z model. More precisely, ten different crystallographic orientations (Fig. 11) are chosen within the list of 240 orientations, using an isotropic texture. A monotonic tensile test (conducted in the hoop direction) is simulated. For the ten different orientations chosen, the stress and strain are computed during the simulation for both the B–Z and the C–P models. Using a mean square minimization procedure, the two parameters, D and δ, are adjusted, and the difference between the stress and strain computed by the B–Z and the C–P models for the ten orientations is minimized. Since the B–Z model is a self-consistent model based on the ‘‘secant approximation”, the Cailletaud–Pilvin (C–P) model is therefore very close, both at the micro and at the macroscopic scale, to the self-consistent ‘‘secant” response. Then, thanks to this adjustment, cyclic tests can be computed. Furthermore, the authors have also proposed to extrapolate the C–P model to non-isotropic textures, which is the case of zirconium alloys. However, since the B–Z model is restricted to elasto-plastic behavior, they decided to use quasi-elastoplastic constitutive laws, with very low strain rate sensitivity.

The computation occurs in several steps. First, from knowledge of the loading (six components of either stress or strain tensors) and of the current macroscopic plastic strain ($\underline{\underline{E}}^p$), the macroscopic stress tensor $\underline{\underline{\Sigma}}$ is deduced from the generalized Hooke's law (Eq. 10).

$$\underline{\underline{\Sigma}} = \sum_{g \in G} f_g \underline{\underline{\sigma}}_g = 2\mu \left\{ \mathbf{I} + \frac{\nu}{1-2\nu} \underline{\underline{I}} \otimes \underline{\underline{I}} \right\} \left(\underline{\underline{E}} - \underline{\underline{E}}^p \right) \qquad (10)$$

Then, from the concentration rule (equation 9) and knowledge of the current value of the internal variable $\underline{\underline{\beta}}_g$ and its average over the whole polycrystal ($\underline{\underline{B}}$), the local stress ($\underline{\underline{\sigma}}_g$) in each crystallographic phase is deduced. At the grain scale, the resolved shear stress is computed for each slip system, according to equation 11.

$$\tau_s = \frac{1}{2} \underline{\underline{\sigma}}_g : \left(\underline{n}_s \otimes \underline{m}_s + \underline{m}_s \otimes \underline{n}_s \right) \qquad (11)$$

In equation 11, $\underline{n}_s$ is the normal of the considered slip system and $\underline{m}_s$ is the glide direction of the considered slip system.

Then, from knowledge of the constitutive law expressed at the slip system scale ($\dot{\gamma}_s = f(\tau_s, ...)$), the shear strain rate for each slip system is deduced. Eventually, the plastic strain rate tensor is computed for the crystallographic phase according to equation 12.

$$\underline{\underline{\dot{\varepsilon}}}_g^p = \frac{1}{2} \sum_{s \in S} \dot{\gamma}_s \left(\underline{n}_s \otimes \underline{m}_s + \underline{m}_s \otimes \underline{n}_s \right) \qquad (12)$$

Finally, when this calculation has been done for every crystallographic phase (g), the overall macroscopic plastic strain rate can be computed with Eq. (13).

$$\underline{\underline{\dot{E}}}^p = \sum_{g \in G} f_g \underline{\underline{\dot{\varepsilon}}}_g^p \qquad (13)$$

A time integration algorithm is then used to compute the new values of all internal variables and all plastic shear strains at the next time step.

Deformation modes

Four types of slip systems are taken into account in the model:

- the three prismatic slip systems with <a> Burgers vector (P),
- the three basal slip systems with <a> Burgers vector (B),
- the six first order pyramidal slip systems with <a> Burgers vector (Πa),
- the twelve first order pyramidal slip systems with <c+a> Burgers vector (Πc).

Crystallographic orientations set used for the simulation

The crystallographic texture (figure 1) of the material is represented by a set of 240 crystallographic orientations (figure 10). It has been verified that the results are only slightly affected by introducing an extensively refined orientations set (less than 3% decrease in hoop flow stress in the case of internal pressure loading).

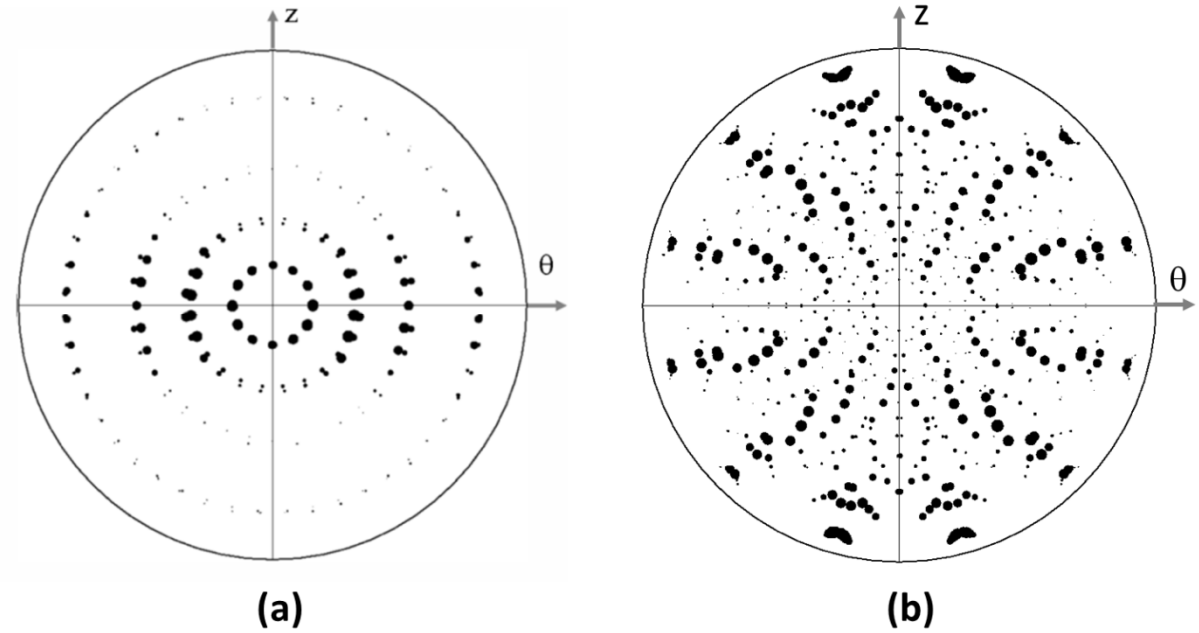

Figure 10: Discretized a) $\{0002\}$ and b) $\{1\bar{1}20\}$ pole figures representative of the texture of the material.

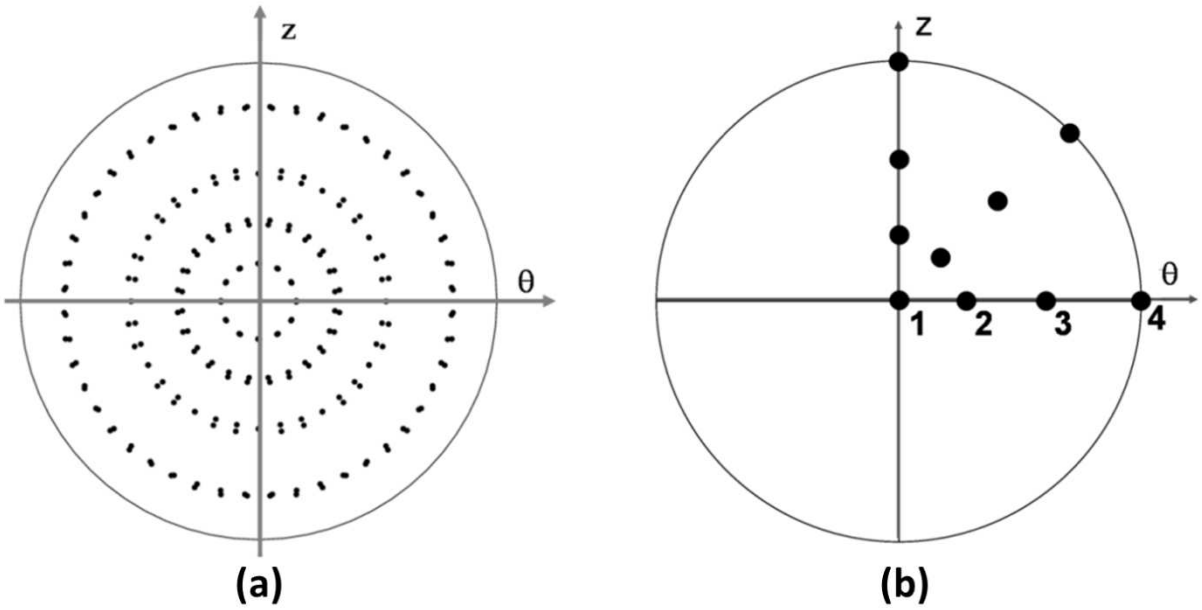

Figure 11: a) Discretized $\{0002\}$ pole figure of the isotropic crystallographic orientation set used for the adjustment of the P-C model on the B-Z model. b) $\{0002\}$ pole figure for the ten orientations used to perform the adjustment during a tensile test conducted in the hoop direction. Four of the ten orientations are numbered. The stress – plastic strain curves of these four orientations are shown below.

Constitutive behavior equations for the non-irradiated recrystallized zirconium alloy

The flow law chosen for the non-irradiated recrystallized zirconium alloy is a Norton-like flow law [35, 36], with a threshold stress (τ_s^c) (equation 14).

$$\dot{\gamma}_s = \left\langle \frac{|\tau_s| - \tau_s^c}{K} \right\rangle^n \mathrm{sign}(\tau_s), \text{ with } \langle x \rangle = x \text{ if } x \geq 0, \langle x \rangle = 0 \text{ if } x < 0 \quad (14)$$

The function $\mathrm{sign}(x)$ can be defined as $\mathrm{sign}(x) = x/|x|$ and gives the sign of x. The parameters, n and K, chosen for this flow law ($K = 5$ MPa and $n = 10$) are such that the model exhibits a very low strain rate sensitivity. With these coefficients, an increase in the applied strain rate from 10^{-6} s^{-1} to 10^{-4} s^{-1} induces an increase in the flow stress of less than 1 MPa at 0.2% plastic strain. This ensures that the chosen model is quasi elasto-plastic, which is a condition needed to apply the B-Z model. These parameters are kept fixed in the following.

The threshold stress, or critical resolved shear stress, is expressed as a simple Taylor expression for the strain hardening (equation 15).

$$\tau_s^c = \tau_s^{c0} + \alpha_d \mu b_s \sqrt{\rho_{tot}} \quad \text{with} \quad \rho_{tot} = \sum_s \rho_s \quad (15)$$

The Burgers vector length is equal to $b_s = a \quad \forall s \in < a >$ for the slip systems with <a> Burgers vector and is equal to $b_s = 1.88a \quad \forall s \in \Pi c$ for slip systems with <c+a> Burgers vector.

The dislocation density evolution for all slip systems is modeled using equation 16.

$$\frac{d\rho_s}{dt} = \frac{|\dot{\gamma}_s|}{b_s}\left(\frac{1}{\lambda} - 2y\rho_s\right) \text{ with } \rho_s(0) = \rho_0 \quad \forall \text{s} \quad (16)$$

This model has only seven coefficients that must be adjusted on the experimental behavior of the material: four initial critical resolved shear stresses ($\tau_P^{c0}, \tau_{\pi a}^{c0}, \tau_B^{c0}, \tau_{\pi c}^{c0}$), two parameters for the evolution of the dislocation densities (λ , y), and one parameter for the effective strength of the dislocation – dislocation interaction (α_d). The elastic properties are based on the experimental analysis. They are chosen as $E = 80$ GPa for the Young's modulus, and $\nu = 0.4$ for the Poisson's ratio and are kept fixed. The initial dislocation density is considered to be equal for every slip system and is assumed to be $\rho_0 = 9.6\times10^{10}$ m^{-2}. Since there are 24 possible slip systems in this model, the total initial dislocation density is equal to $\rho_{tot}(0) = 2.3\times10^{12}$ m^{-2} which is a reasonable value for recrystallized zirconium alloys. Two other parameters, D and δ, must also be adjusted simultaneously on the response obtained, using the isotropic texture, with the B-Z model.

Simulation procedure for the strain path change tests and fitting of the parameters

The mechanical tests have been simulated using the Sidolo software, which was developed by Pilvin [40] and is described in [41]. The quasi-biaxial approach has been adopted for the simulation of the tests. Within this framework, a biaxial stress tensor is used, as explained in the Appendix.

The tests are computed with constant axial strain rate for axial tensile tests or with constant hoop strain rate for internal pressure tests or pure hoop tensile tests, in agreement with the experiments. For internal pressure tests, the axial stress must be equal to half of the hoop stress. But the hoop stress is initially unknown since it is the outcome of the simulation. Therefore, an iterative procedure has been adopted where the tests are simulated several times before converging to the required biaxiality ratio. Furthermore, a specific procedure ensures that each step starts and ends with zero stress, as for the experiment, and that each step smoothly follows its predecessor.

The evaluation of the agreement between simulation and experiment has been done mainly by comparing the flow stress values for each step as a function of the isotropic equivalent cumulated plastic strain.

Starting from the previous parameters obtained with simplified constitutive laws [13], the strain hardening parameters and the critical resolved shear stresses have been adjusted for the behavior of the non-irradiated material. Initially, only the first monotonic steps of each test are computed,

compared with the experiment and used for the refinement. The coefficients D and δ, are also adjusted simultaneously. Then some parameters are only slightly modified to obtain the correct strain hardening along the full cyclic test. The values obtained for each parameter are given in Table 2.

Table 2: Parameters and values obtained after refinement for the non-irradiated material.

Parameter (unit)	Value for non-irradiated material
E (MPa)*	80000
ν (-)*	0.4
n (-)*	10
K ($\mathrm{MPa.s^{1/n}}$)*	5
D (-)	370
δ (-)	0.266
τ_P^0 (MPa)	33
$\tau_{\pi a}^0$ (MPa)	45
τ_B^0 (MPa)	62
$\tau_{\pi c}^0$ (MPa)	102
α_d (-)	0.1
λ (µm)	0.1
y (nm)	9
$\rho_s(0)$ ($\mathrm{m^{-2}}$)*	9.6×10^{10}

The values obtained for the critical resolved shear stresses (τ_P^0 =33 MPa, $\tau_{\pi a}^0$ =45 MPa, τ_B^0 =62 MPa, $\tau_{\pi c}^0$ =102 MPa) are in good agreement with the values adopted by Brenner for the initial critical resolved shear stresses for a Zr-1%Nb-O (alloy A) recrystallized zirconium alloys tested at 673 K. The forest hardening coefficient fitted on the experimental results (α_d =0.1) is slightly lower than the coefficient given by Douglass [26] (α_d =0.28) for crystal bar zirconium. This could be attributed to the lower ability to form junctions in Zy-4 than in crystal bar, as discussed in [26]. The mean free path for dislocation glide should be of the order of half the mean distance between dislocations, which is 0.33 µm in correct agreement with the value of 0.1 µm obtained from the fitting. The annihilation distance adopted of 9 nm is in agreement with values measured for stainless steels [21] on the order of 10 nm.

Results of the simulations and discussion

The results of the simulation of the behavior of recrystallized Zy-4 are shown as black dotted lines in figures 3, 6 and 7.

The simulated flow stress, as a function of the cumulated equivalent plastic strain, for the four tests is compared with the experiment in figures 6 and 7. It can be seen that a fair overall agreement is

obtained between the experiment and the modeling. When considering the first steps, a good agreement is obtained when comparing the yield stress simulated and measured for 0.1% equivalent plastic strain. The simulated yield stress for axial tension, hoop tension test and internal pressure are respectively 104 MPa, 140 MPa and 186 MPa which has to be compared with 117.5 MPa (mean value), 143 MPa and 189 MPa. A very good agreement is also obtained for the flow stress during pure hoop tension. For the internal pressure tests, the predicted flow stress is only 9 MPa below the experimental value (3% error). For the axial tensile tests, the predicted flow stress is about 15 MPa lower than the experimental value (7% error).

The subsequent steps are also predicted well, the kinematic and isotropic hardening being well reproduced by the model. The remaining discrepancies may be partly attributed to more complex interactions between slip systems than the simple Taylor hardening law chosen.

It can also be seen in figure 12 that there is a good agreement between the simulations conducted with the B-Z model and the C-P model, using an isotropic texture, thus ensuring that the C-P model is close to a self-consistent model.

In order to validate the model, a tension-compression test performed by Delobelle et al. [11] in the axial direction on recrystallized Zy-4 has been simulated and compared with the experiment in Figure 13. A good agreement with the experiment can be noticed, thereby confirming the prediction of the kinematic and isotropic hardening of recrystallized zirconium alloys.

However, it can be seen in Figure 3 that the prediction of the strain path is only correct in the case of pure hoop tension (the first step of test HT-AT or the second step of test AT-HT). All the other strain paths are not correctly predicted. This is probably due to a bad prediction of the slip system activities. Indeed, for pure hoop tensile tests, the slip system activities at the end of the loading (2% total hoop strain) are equal to 28% for prismatic slip, 9% for pyramidal <c+a> slip, 24% for basal slip, and 39% for pyramidal <a> slip. In this case, the pyramidal <a> slip seems to be overestimated and the prismatic slip underestimated, since it is known that the prismatic slip is the easy slip system. For internal pressure tests, the prismatic slip activity is only 5%, the pyramidal <c+a> slip is 30%, the basal slip activity is 48%, and the pyramidal <a> slip is 17%. Here, again, the secondary slip system activities are clearly overestimated compared to the activity of the prismatic slip. This problem was already pointed out in a previous work [13]. Concerning axial tensile tests, the prismatic slip activity is 60%, the pyramidal <c+a> is 3%, the basal activity is 5%, and the pyramidal <a> is 32%. These last slip system activities seem to be correct. Further improvements are needed to obtain a better agreement both on the macroscopic response but also on the slip system activities. These numerical improvements must

be done jointly with a thorough experimental analysis of slip system activity using TEM observations or other experimental techniques.

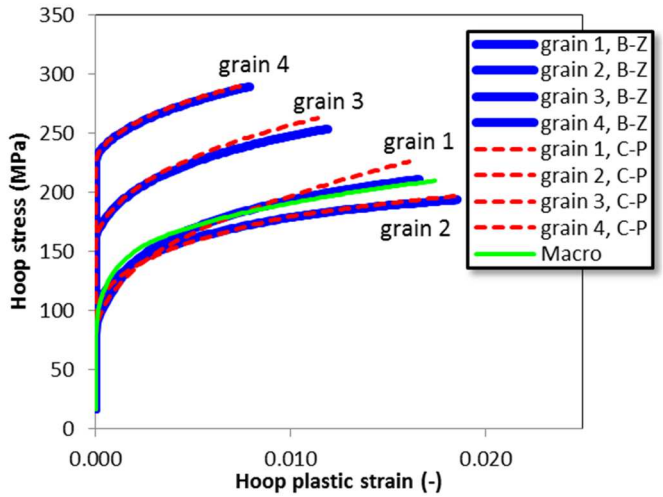

Figure 12 : Comparison between the stress – plastic strain curves simulated by the C-P model and the B-Z model for four specific crystallographic orientations.

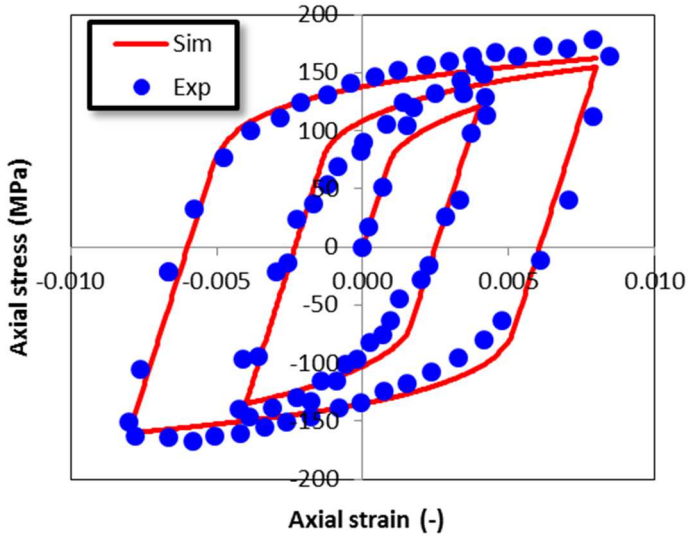

Figure 13 : Simulation of a tension-compression test performed in the axial direction on a recrystallized Zy-4 sample at 623 K by Delobelle et al. [11]. The simulation is shown in continuous red line and the experimental points are shown as the filled blue dots.

Conclusions and outlook

Strain path change tests have been conducted at 623 K on thin tube samples made of recrystallized Zy-4. The tests exhibit evidence of kinematic hardening as well as isotropic hardening. The isotropic

hardening is attributed to the dislocation multiplication and the dislocation –dislocation interactions. The kinematic hardening is attributed to the interaction of the grains with each other.

A polycrystalline model has been used and improved in order to simulate the tests. After refinement, a fair agreement is obtained between the macroscopic simulated and experimental behaviors. In particular, the isotropic and kinematic hardenings are well predicted by the model. However, the strain paths are not well predicted, which is probably due to a poor prediction of the slip system activities.

Further improvements must be made. On the numerical side, a better prediction of the slip system activities and strain paths are needed. On the experimental side, accurate quantifications of slip system activities are required.

The effect of neutron irradiation on the response of the material to change of loading path must also be studied. This would bring a new insight in the strain hardening behavior of neutron irradiated zirconium alloys that will eventually enable the development of predictive models for the in reactor deformation.

Appendix : Analysis of the mechanical tests

It can be shown that when the external pressure is negligible compared to the inner pressure, the mean stress tensor in the thickness of the tube is expressed as equation A-1. In equation A-1, P is the internal pressure, F the external applied force, r_e is the external radius of the tube, r_i the internal radius of the tube and e the thickness of the tube ($r_e = r_i + e$).

$$\underline{\underline{\sigma}} = P\begin{bmatrix} -r_i/(r_i+r_e) & 0 & 0 \\ 0 & r_i/e & 0 \\ 0 & 0 & r_i^2/(r_e^2-r_i^2) \end{bmatrix} + F\begin{bmatrix} 0 & 0 & 0 \\ 0 & 0 & 0 \\ 0 & 0 & 1/\left[\pi(r_e^2-r_i^2)\right] \end{bmatrix} \quad \text{(A-1)}$$

By defining the geometrical parameter η as $\eta = e/D_m$, the stress tensor can be expressed as equation A-2. D_m is the mean diameter defined as $D_m = (D_i + D_e)/2 = D_e - e$, D_i is the inner diameter and D_e the external diameter.

$$\underline{\underline{\sigma}} = \frac{PD_m}{2e}\begin{bmatrix} -\eta-\eta^2 & 0 & 0 \\ 0 & 1-\eta & 0 \\ 0 & 0 & 1/2-\eta+\eta^2 \end{bmatrix} + \frac{F}{e\pi D_m}\begin{bmatrix} 0 & 0 & 0 \\ 0 & 0 & 0 \\ 0 & 0 & 1 \end{bmatrix} \quad \text{(A-2)}$$

For the thin cladding tube considered here ($\eta = e/D_m = 0.57/(9.5-0.57) = 0.064 = 6.4\%$) the second order approximation in η gives a very good evaluation of the mean stress tensor in the wall of the tube (equation A-3).

$$\underline{\underline{\sigma}} = \frac{PD_m}{2e}\begin{bmatrix} -\eta & 0 & 0 \\ 0 & 1-\eta & 0 \\ 0 & 0 & 1/2-\eta \end{bmatrix} + \frac{F}{e\pi D_m}\begin{bmatrix} 0 & 0 & 0 \\ 0 & 0 & 0 \\ 0 & 0 & 1 \end{bmatrix} + O\left(\eta^2\right) \text{(A-3)}$$

On the other hand the first order approximation, which corresponds to the thin wall formula, gives a poor approximation for the stress tensor (equation A-4).

$$\underline{\underline{\sigma}} = \frac{PD_m}{2e}\begin{bmatrix} 0 & 0 & 0 \\ 0 & 1 & 0 \\ 0 & 0 & 1/2 \end{bmatrix} + \frac{F}{e\pi D_m}\begin{bmatrix} 0 & 0 & 0 \\ 0 & 0 & 0 \\ 0 & 0 & 1 \end{bmatrix} + O(\eta) \quad \text{(A-4)}$$

It is worth pointing out that the deviatoric stress (defined as $\underline{\underline{s}} = \underline{\underline{\sigma}} - \frac{1}{3}\mathrm{tr}(\underline{\underline{\sigma}})\underline{\underline{I}}$) computed with the first order approximation is equal to the deviatoric stress computed with the second order approximation. This is an important point since the plastic deformation, which occurs with constant volume is only sensitive to the deviatoric part of the stress tensor.

The Hill's equivalent stress can be written in the general case as equation A-5.

$$\sigma_H^{eq} = \sqrt{H_1(\sigma_{\theta\theta}-\sigma_{zz})^2 + H_2(\sigma_{zz}-\sigma_{rr})^2 + H_3(\sigma_{rr}-\sigma_{\theta\theta})^2 + 2H_4\sigma_{r\theta}^2 + 2H_5\sigma_{rz}^2 + 2H_6\sigma_{\theta z}^2} \quad \text{(A-5)}$$

Equation A-5 reduces to equation A-6, considering that the non-diagonal terms of the stress tensor are equal to zero.

$$\sigma_H^{eq} = \sqrt{H_1\left(\sigma_{\theta\theta} - \sigma_{zz}\right)^2 + H_2\left(\sigma_{zz} - \sigma_{rr}\right)^2 + H_3\left(\sigma_{rr} - \sigma_{\theta\theta}\right)^2} \qquad \text{(A-6)}$$

In equation A-5, the reference direction is often taken as the axial direction, which leads $H_1 + H_2 = 1$, so that for axial tensile test the Hill's equivalent stress is equal to the axial stress. From equation A-6 it can be seen that when the stress components are replaced either by the first order approximation or the second order approximation stress tensor components, the Hill's equivalent stress are equal.

It can be seen, from equation A-3, that the stress state in the wall of the tube has in fact three components. However, the component along the radial direction remains small compared to the two others. It is therefore convenient, in order to remain consistent with the thin wall approximation, to analyze this mechanical test by defining a "quasi-biaxial" (with superscript "*qb*") hoop stress ($\sigma_{\theta\theta}^{qb}$) and a "quasi-biaxial" axial stress (σ_{zz}^{qb}) as (equation A-7) :

$$\sigma_{\theta\theta}^{qb} = \sigma_{\theta\theta} - \sigma_{rr} = \frac{PD_m}{2e} \text{ and } \sigma_{zz}^{qb} = \sigma_{zz} - \sigma_{rr} = \frac{PD_m}{4e} + \frac{F}{e\pi D_m} \qquad \text{(A-7)}$$

In this approach the mechanical test is analyzed as a quasi-biaxial test where the plane *P* $\left(\sigma_{\theta\theta}, \sigma_{zz}\right)$ used when analyzing a biaxial test in the stress space is replaced by a plane *P'* only slightly tilted in the stress space with a normal vector $\underline{n} = \left[1-\eta, \eta, 0\right]$. Within this framework the stress state of an internal pressure test performed without external force ($F = 0$) follows a line in the plane *P'* along the vector $\underline{u} = \left[-\eta, 1-\eta, 1/2-\eta\right]$, with $\sigma_{zz}^{qb} / \sigma_{\theta\theta}^{qb} = 1/2$. In that case, the actual biaxiality ratio is $\alpha = \sigma_{zz} / \sigma_{\theta\theta} = \left(1/2-\eta\right)/\left(1-\eta\right)$=0.47. The axial test performed with a biaxiality ratio of $\alpha = \sigma_{zz} / \sigma_{\theta\theta}$=100 follows a line along the vector $\underline{u} = \left[-\eta, 1-\eta, 100\times\left(1-\eta\right)\right]$, with $\sigma_{zz}^{qb} / \sigma_{\theta\theta}^{qb} = \left(1-\eta\right)\alpha + \eta$ =93.7. The pure hoop tensile test performed with the biaxiality ratio of $\alpha = \sigma_{zz} / \sigma_{\theta\theta} = 0$ follows a line along the vector $\underline{u} = \left[-\eta, 1-\eta, 0\right]$, with $\sigma_{zz}^{qb} / \sigma_{\theta\theta}^{qb} = \eta$ =0.064. In this work, the mechanical tests are analyzed in the plane *P'* by plotting $\sigma_{\theta\theta}^{qb}$ and σ_{zz}^{qb} . This is referred to as the "quasi-biaxial" approach. It can be noted that the quasi-biaxial hoop stress ($\sigma_{\theta\theta}^{qb} = \sigma_{\theta\theta} - \sigma_{rr}$) corresponds to the Tresca equivalent stress.

Concerning the numerical simulation described in this article, the quasi-biaxial approach can also be used by applying a biaxial stress tensor with the biaxiality ratio $\sigma_{zz}^{qb} / \sigma_{\theta\theta}^{qb}$. Indeed, the deviatoric stress in this "quasi-biaxial" approach is equal to the deviatoric stress using the triaxial stress tensor. In that

case the computed hoop and axial stress can be directly compared to the experimental values of $\sigma_{\theta\theta}^{qb}$ and σ_{zz}^{qb}.

The engineering axial strain (with superscript "eng") is computed according to the formula given in equation A-8.

$$\varepsilon_{zz}^{eng} = \frac{\Delta L}{L_0} \qquad \text{(A-8)}$$

Concerning the hoop strain, since it is not homogeneous through the thickness of the tube, it is necessary to compute the mean hoop strain. However, only the evolution of the external diameter is measured during the test. A good evaluation of the mean hoop strain is obtained by dividing the evolution of the external diameter by the initial mean diameter (equation A-9).

$$\varepsilon_{\theta\theta}^{eng} = \frac{\Delta D_m}{D_m(0)} \approx \frac{\Delta D_{ext}}{D_m(0)} = \frac{\Delta D_{ext}}{D_{ext}(0) - e(0)} \qquad \text{(A-9)}$$

The quantities given above are engineering stress and strain. In order to compute the true stress (with superscript "true") it is necessary to take into account the evolution of the gauge length and the evolution of the thickness and mean diameter throughout the test. The true axial and hoop strains are computed according to equation A-10.

$$\varepsilon_{zz}^{true} \approx \ln\left(1+\varepsilon_{zz}^{eng}\right) \text{ et } \varepsilon_{\theta\theta}^{true} \approx \ln\left(1+\varepsilon_{\theta\theta}^{eng}\right) \qquad \text{(A-10)}$$

The axial and hoop true stresses are therefore computed (written within the "quasi-biaxial" approach) according to equation A-11 and A-12.

$$\left(\sigma_{zz}^{true}\right)_{qb} = \sigma_{zz}^{true} - \sigma_{rr}^{true} = \left(\sigma_{zz}^{eng}\right)_{qb}\left(1+\varepsilon_{zz}^{eng}\right) \quad \text{(A-11)}$$

$$\left(\sigma_{\theta\theta}^{true}\right)_{qb} = \sigma_{\theta\theta}^{true} - \sigma_{rr}^{true} = \sigma_{\theta\theta}^{eng}\frac{\exp\left(\varepsilon_{\theta\theta}^{true}\right)}{\exp\left(\varepsilon_{rr}^{true}\right)} = \sigma_{\theta\theta}^{qb}\left(1+\varepsilon_{\theta\theta}^{eng}\right)^{1+K_0} \text{ with } K_0 = -\varepsilon_{rr}^{true}/\varepsilon_{\theta\theta}^{true} \qquad \text{(A-12)}$$

In this work the experimental results are plotted using true stress and strain, in the framework of the quasi-biaxial approach, assuming a value of $K_0 = 0$ for a simplified analysis (equation A-13) (a value of $K_0 = 1$ corresponds to an isotropic behavior).

$$\left(\sigma_{\theta\theta}^{true}\right)_{qb} = \sigma_{\theta\theta}^{true} - \sigma_{rr}^{true} \approx \sigma_{\theta\theta}^{qb}\left(1+\varepsilon_{\theta\theta}^{eng}\right) \quad \text{(A-13)}$$

From these biaxial tests, the elastic properties of the material can also be evaluated. For axial tensile tests the elastic slope corresponds to the Young's modulus (E) and the Poisson's ratio can be measured as $\nu = -\dot{\varepsilon}_{\theta\theta}/\dot{\varepsilon}_{zz}$ in the elastic domain. For internal pressure tests, using the exact stress tensor given in equation A-1, it can be shown that hoop and radial stress gradient within the tube wall have an exact analytical solution. The elastic behavior can therefore be deduced exactly with the elastic strain measured on the external diameter of the tube. It can be shown that the hoop stress is related

to the hoop strain defined above by the apparent elastic modulus (E_{app}) during internal pressure test (equation A-14).

$$E_{app} = \frac{E}{(1-\eta)(1-\nu/2)} \quad \text{(A-14)}$$

This result is slightly different from the computation of the elastic slope from the quasi-biaxial approach, using the mean strain and stress in the thickness of the tube. The correct formula to use is equation A-14.

In the case of internal pressure test, a good approximation of the Poisson's ratio is given by equation A-15.

$$\nu = (1-2\dot{\varepsilon}_{zz}/\dot{\varepsilon}_{\theta\theta})/(2-\dot{\varepsilon}_{zz}/\dot{\varepsilon}_{\theta\theta}) \qquad \text{(A-15)}$$

References

[1] Michel, B., Sercombe, J., Nonon, C., Fandeur, O. (2012). Modeling of Pellet Cladding Interaction, Chapter 3.22 in : Comprehensive Nuclear Materials, Elsevier, R. Könings Ed., 3, 677-712.

[2] Bessiron, V., Jamet, N., Gressier, C., Schuh, K.-D., Sautereau, A., Paul, T., Royere C. (2014) AREVA's PCI Methodologies for PWR Enhanced Plant Maneuverability. Proceedings of WRFPM 2014, Sendai, Japan, Sep. 14-17, 2014.

[3] Michel, B., Sercombe, J., Thouvenin, G. (2008). A new phenomenological criterion for pellet–cladding interaction rupture. Nuclear Engineering and Design, 238(7), 1612-1628.

[4] Miller A.K. (1987). Unified Constitutive Equations for Creep and Plasticity, Alan K. Miller Ed., Elsevier Applied Science Ltd, Springer Netherlands.

[5] Lemaitre, J., Chaboche, J.-L. (1990). Mechanics of solid materials, Cambridge University Press.

[6] Chaboche, J.L., (1989). Constitutive equations for cyclic plasticity and cyclic viscoplasticity, International Journal of Plasticity, 5, 247-302.

[7] Chaboche, J.L. (2008). A review of some plasticity and viscoplasticity constitutive theories, International Journal of Plasticity, 24, 1642–1693

[8] MacEwen, S. R., Ells, C. E., Woo, O. T. (1981). The Bauschinger effect in Zircaloy-2, J. Nucl. Mater., 101(3), 336-349.

[9] Christodoulou, N. (1989). Evolution of the Bauschinger effect in tension and compression in Zircaloy-2. Acta Metallurgica, 37(2), 529-539.

[10] Wisner, S. B., Reynolds, M. B., Adamson, R. B. (1994). Fatigue behavior of irradiated and unirradiated zircaloy and zirconium. In Zirconium in the Nuclear Industry: Tenth International Symposium. ASTM International. ASTM STP, *1245*, 499-520.

[11] Delobelle, P., Robinet, P., Geyer, P., Bouffioux, P. (1996). A model to describe the anisotropic viscoplastic behaviour of Zircaloy-4 tubes. J. Nucl. Mater., 238(2), 135-162.

[12] Li, C., Ying, S., Shen, B., Qiu, S., Ling, X., Wang, Y.,Peng, Q. (2003). Cyclic stress–strain response of textured Zircaloy-4. J. Nucl. Mater., 321(1), 60-69.

[13] Onimus, F., Béchade, J.-L. (2009). A polycrystalline modeling of the mechanical behavior of neutron irradiated zirconium alloys, J. Nucl. Mater., 384(2), 163-174.

[14] Onimus, F., Béchade, J.-L., Gilbon, D. (2013). Experimental analysis of slip systems activation in neutron irradiated zirconium alloys and comparison with polycrystalline model simulations, Metallurgical and Materials Transactions A., 44(1), 45 – 60.

[15] Bernachy-Barbe, F., Gélébart, L., Bornert, M., Crépin, J., Sauder, C. (2015). Anisotropic damage behavior of SiC/SiC composite tubes: Multiaxial testing and damage characterization. Composites Part A: Applied Science and Manufacturing, 76, 281-288.

[16] Limon, R., Lehmann, S. (2004). A creep rupture criterion for Zircaloy-4 fuel cladding under internal pressure, J. Nucl. Mater., 335, 322–334.

[17] Cappelaere, C., Limon, R., Duguay, C., Pinte, G., Le Breton, M., Bouffioux, P., Chabretou, V., Miquet, A., (2012). Thermal creep model for CSWR Zircaloy-4 cladding taking into account the annealing of the irradiation hardening, Nuclear Technology, 177, 257-272.

[18] Northwood, D. O., Rosinger, H. E. (1980). Influence of oxygen on the elastic properties of Zircaloy-4. Journal of Nuclear Materials, 89(1), 147-154.

[19] Schwenk, E. B., Wheeler, K. R., Shearer, G. D., Webster, R. T. (1978). Poisson's ratio in zircaloy-4 between 24° and 316° C. Journal of Nuclear Materials, 73(1), 129-131.

[20] Povolo, F., Bolmaro, R. E. (1983). Poisson's ratio in zirconium single crystals. Journal of Nuclear Materials, 118(1), 78-82.

[21] Feaugas, X. (1999). On the origin of the tensile flow stress in the stainless steel AISI 316L at 300 K: back stress and effective stress. Acta materialia, 47(13), 3617-3632.

[22] Dickson, J.L., Boutin, J., Handfield, L. (1984). A comparison of two simple methods for measuring cyclic internal and effective stresses. Mat. Sci. Eng., A64, L7–L11

[23] Le Saux, M., Besson, J., Carassou, S., Poussard, C., Averty, X. (2008). A model to describe the anisotropic viscoplastic mechanical behavior of fresh and irradiated Zircaloy-4 fuel claddings under RIA loading conditions. Journal of Nuclear Materials, 378(1), 60-69.
[24] Rautenberg, M., Poquillon, D., Pilvin, P., Grosjean, C., Cloué, J. M., Feaugas, X. (2014). Thermal isocreep curves obtained during multi-axial creep tests on recrystallized Zircaloy-4 and M5™ alloy. Nuclear Engineering and Design, 269, 33-37.
[25] Aqua, N., Owens, CM. (1967). The Microstructural Characterization of Cold-Rolled Zircaloy-4 Sheet. Trans. Met. Soc. AIME 239 155.
[26] Douglass, D. L. (1971). Metallurgy of Zirconium. Atomic Energy Review, Supplement, IAEA, Vienna, Austria.
[27] Monnet, G., Devincre, B., Kubin, L. P. (2004). Dislocation study of prismatic slip systems and their interactions in hexagonal close packed metals: application to zirconium. Acta materialia, 52(14), 4317-4328.
[28] Tenckhoff, E. (1988). Deformation Mechanisms, Texture, and Anisotropy in Zirconium and Zircaloy, ASTM, STP Vol. 966, ASTM International, West Conshohocken, PA, USA.
[29] Kocks, U. F., Tomé, C. N., Wenk, H. R. (2000). Texture and Anisotropy, Preferred Orientations in Polycrystals and their Effect on Materials Properties, Cambridge University Press.
[30] Feaugas, X., Gaudin, C. (2001). Different levels of plastic strain incompatibility during cyclic loading: in terms of dislocation density and distribution. Materials Science and Engineering: A, 309, 382-385.
[31] Bornert, M., Bretheau, T., Gilormini, P. (2001). Homogénéisation en mécanique des matériaux, Tome 1: Matériaux aléatoires élastiques et milieux périodiques.
[32] Turner, P. A., Christodoulou, N., Tomé, C. N. (1995). Modeling the mechanical response of rolled zircaloy-2. International journal of plasticity, 11(3), 251-265.
[33] Brenner, R., Masson, R., Castelnau, O., Zaoui, A. (2002). A “quasi-elastic” affine formulation for the homogenised behaviour of nonlinear viscoelastic polycrystals and composites. European Journal of Mechanics-A/Solids, 21(6), 943-960.
[34] Berveiller, M., Zaoui, A. (1978). An extension of the self-consistent scheme to plastically-flowing polycrystals. Journal of the Mechanics and Physics of Solids, 26(5), 325-344.
[35] Hoc, T., Forest, S. (2001). Polycrystal modelling of IF-Ti steel under complex loading path. International Journal of Plasticity, 17(1), 65-85.
[36] Cailletaud, G. (1992). A micromechanical approach to inelastic behaviour of metals. International Journal of Plasticity, 8(1), 55-73.
[37] Pilvin, P. (1994). Proceedings of the International Conference on Biaxial/Multiaxial Fatigue, pp. 31-46, ESIS/SF2M, Saint-Germain en Laye, France, 1994.
[38] Feaugas, X., Pilvin, P., Clavel, M. (1997). Cyclic deformation behaviour of an α/β titanium alloy—II. Internal stresses and micromechanic modelling. Acta Mater., 45(7), 2703–2714.
[39] Priser, M., Rautenberg, M., Cloué, J.-M., Pilvin, P., Feaugas, X. Poquillon, D. (2011). Multiscale Analysis of Viscoplastic Behavior of Recrystallized Zircaloy-4 at 400° C. In Zirconium in the Nuclear Industry: 16th International Symposium. ASTM International. J. ASTM Int., 8(1), 10-19.
[40] Pilvin, P. (2003). SiDoLo version 2.4495 Notice d’utilisation. Université de Bretagne-Sud.
[41] Andrade-Campos, A., Thuillier, S., Pilvin, P., Teixeira-Dias, F. (2007). On the determination of material parameters